

1 **Distinct Impacts of El Niño-Southern Oscillation and Indian Ocean Dipole**  
2 **on China's Gross Primary Production**

3 Ran Yan<sup>1,2</sup>, Jun Wang<sup>1,2\*</sup>, Weimin Ju<sup>1,2\*</sup>, Xiuli Xing<sup>3</sup>, Miao Yu<sup>4</sup>, Meirong Wang<sup>4</sup>, Jingye

4 Tan<sup>1,2</sup>, Xunmei Wang<sup>1,2</sup>, Hengmao Wang<sup>1,2</sup>, Fei Jiang<sup>1,2</sup>

5 <sup>1</sup>Frontiers Science Center for Critical Earth Material Cycling, International Institute for Earth System Science,  
6 Nanjing University, Nanjing, Jiangsu 210023, China

7 <sup>2</sup>Jiangsu Provincial Key Laboratory of Geographic Information Science and Technology, Key Laboratory for Land  
8 Satellite Remote Sensing Applications of Ministry of Natural Resources, School of Geography and Ocean Science,  
9 Nanjing University, Nanjing, Jiangsu 210023, China

10 <sup>3</sup>Department of Environmental Science and Engineering, Fudan University, No. 2005, Songhu Road, Yangpu  
11 District, Shanghai 200438, China

12 <sup>4</sup>Joint Center for Data Assimilation Research and Applications/Key Laboratory of Meteorological Disaster,  
13 Ministry of Education/Joint International Research Laboratory of Climate and Environment Change (ILCEC)/  
14 Collaborative Innovation Center ON Forecast and Evaluation of Meteorological Disasters, Nanjing University of  
15 Information Science and Technology, Nanjing 210044, China

16 Corresponding author: Jun Wang ([wangjun@nju.edu.cn](mailto:wangjun@nju.edu.cn)); Weimin Ju ([juweimin@nju.edu.cn](mailto:juweimin@nju.edu.cn))

17

18 **Abstract**

19 Gross primary production (GPP) stands as a crucial component in the terrestrial carbon cycle,  
20 greatly affected by large-scale circulation adjustments. This study explores the influence of El  
21 Niño-Southern Oscillation (ENSO) and Indian Ocean Dipole (IOD) on China's GPP, utilizing  
22 long-term GPP data generated by the Boreal Ecosystem Productivity Simulator (BEPS). Partial  
23 correlation coefficients between GPP and ENSO reveal substantial negative associations in  
24 most parts of western and northern China during the September-October-November (SON)  
25 period of ENSO development. These correlations shift to strongly positive over southern China  
26 in December-January-February (DJF), then weaken in March-April-May (MAM) in the  
27 following year, eventually turning generally negative over southwestern and northeastern China  
28 in June-July-August (JJA). In contrast, the relationship between GPP and IOD basically exhibits  
29 opposite seasonal patterns. Composite analysis further confirms these seasonal GPP anomalous  
30 patterns. Mechanistically, these variations are predominantly controlled by soil moisture during  
31 ENSO events (except MAM) and by temperature during IOD events (except SON).  
32 Quantitatively, China's annual GPP demonstrates modest positive anomalies in La Niña and  
33 negative IOD years, in contrast to minor negative anomalies in El Niño and positive IOD years.  
34 This results from counterbalancing effects with significantly greater GPP anomalous  
35 magnitudes in DJF and JJA. Additionally, the relative changes in total GPP anomalies at the  
36 provincial scale display an east-west pattern in annual variation, while the influence of IOD  
37 events on GPP presents an opposing north-south pattern. We believe that this study can  
38 significantly enhance our understanding of specific processes by which large-scale circulation  
39 influences climate conditions and, in turn, affects China's GPP.

40

41 **Key words:** Gross primary production, China, El Niño-Southern Oscillation, Indian Ocean  
42 Dipole, BEPS

43

## 44 **1.Introduction**

45 Vegetation photosynthesis, a pivotal physiological process affecting the terrestrial carbon cycle,  
46 predominantly governs variations in the net biome productivity (NBP), surpassing the impact  
47 of total ecosystem respiration (Piao et al., 2020; Wang et al., 2022; Wang et al., 2018). Gross  
48 primary production (GPP) represents the total amount of carbon dioxide assimilated by plants  
49 per unit time through the photosynthetic processes, acting as a crucial carbon flux in mitigating  
50 anthropogenic CO<sub>2</sub> emissions (Gough, 2012; Houghton, 2007). However, despite evident long-  
51 term increasing trends in GPP, primarily attributed to CO<sub>2</sub> fertilization (Ryu et al., 2019;  
52 Schimel et al., 2015; Yang et al., 2022), it also shows regional and global interannual variations.  
53 These variations are largely linked to climate fluctuations driven by ocean-atmosphere  
54 interactions and the teleconnections (Wang et al., 2021b; Ying et al., 2022). To date, the impact  
55 of such teleconnections on China's GPP remains insufficiently documented.

56  
57 The El Niño-Southern Oscillation (ENSO) exerts a significant influence on the global terrestrial  
58 carbon cycle, which is the dominant mode of inter-annual climate variability (Bauch, 2020;  
59 Kim et al., 2017; Wang et al., 2016; Wang et al., 2018; Zeng et al., 2005). Within this context,  
60 GPP typically assumes a leading role in shaping the response of terrestrial carbon sinks to  
61 ENSO events (Ahlstrom et al., 2015; Wang et al., 2018; Zhang et al., 2018). Global patterns  
62 reveal a negative GPP anomaly of approximately  $-1.08 \text{ Pg C yr}^{-1}$  during El Niño years,  
63 contrasting a positive GPP anomaly of about  $1.63 \text{ Pg C yr}^{-1}$  in La Niña years (Zhang et al.,  
64 2019). However, the impact of ENSO on GPP exhibits significant regional differences. At  
65 present, while existing researches have predominantly focused on the response of tropical GPP  
66 to ENSO, studies specific to China are relatively limited. Liu et al. (2014) highlighted the effects  
67 of ENSO on crop growth in the North China, and Li et al. (2021) demonstrated that the response  
68 of GPP to El Niño varies with the phase of the Pacific Decadal Oscillation (PDO) in the eastern  
69 China.

70  
71 ENSO is not the sole global climatic oscillation, influencing the terrestrial carbon cycle.

72 Another significant player is the Indian Ocean Dipole (IOD), a tropical coupled ocean-  
73 atmosphere mode (Saji et al., 1999), which also affects the terrestrial carbon cycling by  
74 modulating the climate circulations (Wang et al., 2022; Wang et al., 2020; Wang et al., 2021b;  
75 Yan et al., 2023). Research indicates that IOD events can influence precipitation in China, with  
76 effects lasting from the year of the event through the subsequent summer (Zhang et al., 2022a).  
77 Zhang et al. (2022b) also proved that extreme positive IOD (pIOD) events in 2019 affected the  
78 precipitation in summer 2020 in Eastern China, and proposed that the summer precipitation in  
79 the following year was mainly affected by IOD in northern China, while by ENSO in the  
80 Yangtze River Basin. Additionally, a prior study explored the influence of the extreme  
81 pIOD event in 2019 on GPP anomalies across the Indian Ocean rim countries. It suggested a  
82 conspicuous negative GPP anomaly occurred in eastern China during the September-October-  
83 November (SON) (Wang et al., 2021b).

84

85 The primary objective of this study was to comprehensively assess the impact of ENSO and  
86 IOD events on GPP in China. To this end, we initially employed partial correlation analysis to  
87 elucidate the relationship between GPP and climate anomalies, specifically soil moisture and  
88 temperature, induced by ENSO and IOD events across various seasons. The analysis utilized  
89 historical long-term GPP data spanning from 1981 to 2021, simulated by the Boreal Ecosystem  
90 Productivity Simulator (BEPS) model. The aim was to get a preliminary understanding of the  
91 influence exerted by ENSO and IOD. Furthermore, composite analysis was adopted to illustrate  
92 the actual responses during distinct events, including individual ENSO and IOD occurrences.  
93 The ensuing discussion will delve into the analysis results on national, regional, and provincial  
94 scales.

95

## 96 2.Datasets and methods

### 97 2.1 Datasets used

98 The sea surface temperature (SST) dataset was~~are~~ derived from the Monthly NOAA's Extended  
99 Reconstructed Sea Surface Temperature version 5 (ERSSTv5) (Muñoz, 2019). It is generated  
100 on a 2°x2° grid, using statistical methods to enhance spatial completeness. Commencing from  
101 January 1854 to the present, the monthly SST data includes anomalies computed with respect  
102 to a 1971-2000 monthly climatology.

103

104 Meteorological data were adopted from ECMWF Reanalysis v5 (ERA5)-Land monthly  
105 averaged data with 0.1° × 0.1° grids, including 2m surface air temperature (TAS), and  
106 volumetric soil moisture (SM) during the period from 1981 to 2021. ERA5-Land was created  
107 by replaying the land component of the ECMWF ERA5 climate reanalysis at a higher resolution  
108 compared to ERA5. Reanalysis combines model data with global observations into a consistent  
109 dataset based on the laws of physics. The original soil moisture data was divided into four layers  
110 based on different surface depths. These layers were depth-weighted and then aggregated into  
111 the average soil moisture to a depth of 289cm (m<sup>3</sup> m<sup>-3</sup>).

112

113 GPP spanning from 1981 to 2021 was simulated by the BEPS model, featuring a horizontal  
114 resolution of 0.0727° × 0.0727°. The BEPS model, originally developed for Canadian boreal  
115 ecosystems, has been re-constructed for GPP simulations on the global scale (Chen et al., 1999;  
116 Chen et al., 2012). BEPS is a process-based model driven by satellite-observed leaf area index  
117 (LAI) and foliage clumping index ( $\Omega$ ), meteorological data, land cover types, soil texture, and  
118 CO<sub>2</sub> concentration to simulate the daily carbon flux of terrestrial ecosystems (Chen et al., 2019;  
119 Liu et al., 1997). The input data used to drive GPP in this study include ERA5 meteorological  
120 data (Hersbach et al., 2023), GLOBMAP LAI product (Liu et al., 2012), Land Cover  
121 Classification System (LCCS) generated by the Food and Agriculture Organization (FAO) of  
122 the United Nations (Friedl and Sulla-Menashe, 2019), Harmonized World Soil Database v1.2

123 from FAO (Fischer et al., 2008), and CO<sub>2</sub> concentration based on the Global Monitoring  
124 Laboratory from NASA (Lan et al.).

125 Notably, BEPS distinguishes itself from other models through the organic combination of  
126 remote sensing data and mechanistic modelling. It produces simulation datasets for GPP, Net  
127 primary productivity (NPP), and evapotranspiration (ET). Key features of BEPS include the  
128 incorporation of sunlit-shaded leaf stratification strategy (Norman, 1982). The model calculates  
129 canopy-level photosynthesis by summing the GPP of sunlit and shaded leaves (Chen et al.,  
130 1999).

$$131 \quad GPP = A_{sun}LAI_{sun} + A_{shade}LAI_{shade} \quad (1)$$

$$132 \quad LAI_{sun} = 2 \cos \theta \left[ 1 - \exp \left( -\frac{0.5\Omega LAI}{\cos \theta} \right) \right] \quad (2)$$

$$133 \quad LAI_{shade} = 1 - LAI_{sun} \quad (3)$$

134 where  $A_{sun}$  and  $A_{shade}$  represent the amount of photosynthesis at per sunlit and shaded leaf,  
135 respectively;  $LAI_{sun}$  and  $LAI_{shade}$  represent the canopy-level sunlit and shaded LAI,  
136 respectively;  $\Omega$  is the foliage clumping index indicating the influence of foliage clustering on  
137 radiation transmission, and  $\theta$  is the solar zenith angle.

138

139 The accuracy of carbon flux products simulated by BEPS has been validated in previous studies  
140 (Chen et al., 2019; He et al., 2021). We also used the measured site data from ChinaFlux  
141 (<http://chinaflux.org/>) and National Tibetan Plateau Third Pole Environment (Li et al., 2013)  
142 (Table S1) to assess the performance of BEPS simulated GPP (Fig. S1). Our analysis reveals a  
143 high consistency between simulated and observed GPP, with an average R<sup>2</sup> of 0.77 ( $p < 0.05$ )  
144 and an average root mean square error (RMSE) of 1.70 gC m<sup>-2</sup> day<sup>-1</sup>. In addition, the global  
145 terrestrial GPP from FluxSat product Version 2.2 (Joiner et al., 2018) was also used to assess  
146 the reliability of BEPS GPP. FluxSat GPP is obtained by using light-use efficiency (LUE)  
147 framework based on Moderate-resolution Imaging Spectroradiometer (MODIS) satellite data,  
148 eliminating the dependency on other meteorological input data. The comparison between BEPS  
149 GPP and FluxSat GPP data revealed a robust agreement, with a correlation coefficient ( $r$ ) of  
150 0.63 ( $p < 0.05$ ) and a RMSE of 1.1 Pg C yr<sup>-1</sup> (Fig. S2). These consistencies underscore the

151 reliability of the BEPS GPP data in capturing terrestrial carbon flux dynamics.

## 152 **2.2 Anomaly calculation**

153 To calculate anomalies, we initially eliminated the long-term climatology to get rid of the  
154 seasonal cycle. Subsequently, we subtracted the 7-year running average for each grid to  
155 eliminate the decadal oscillation and long-term trends for all the variables. Further, refinement  
156 involved smoothing the derived GPP and climate anomalies using a 3-month running average  
157 to remove the intra-seasonal variability. For consistency, the BEPS simulated GPP data was  
158 resampled to  $0.1^\circ \times 0.1^\circ$ . To align with this, non-vegetated areas in the climate data were  
159 masked according to the resampled BEPS GPP, uniformity in spatial representation.

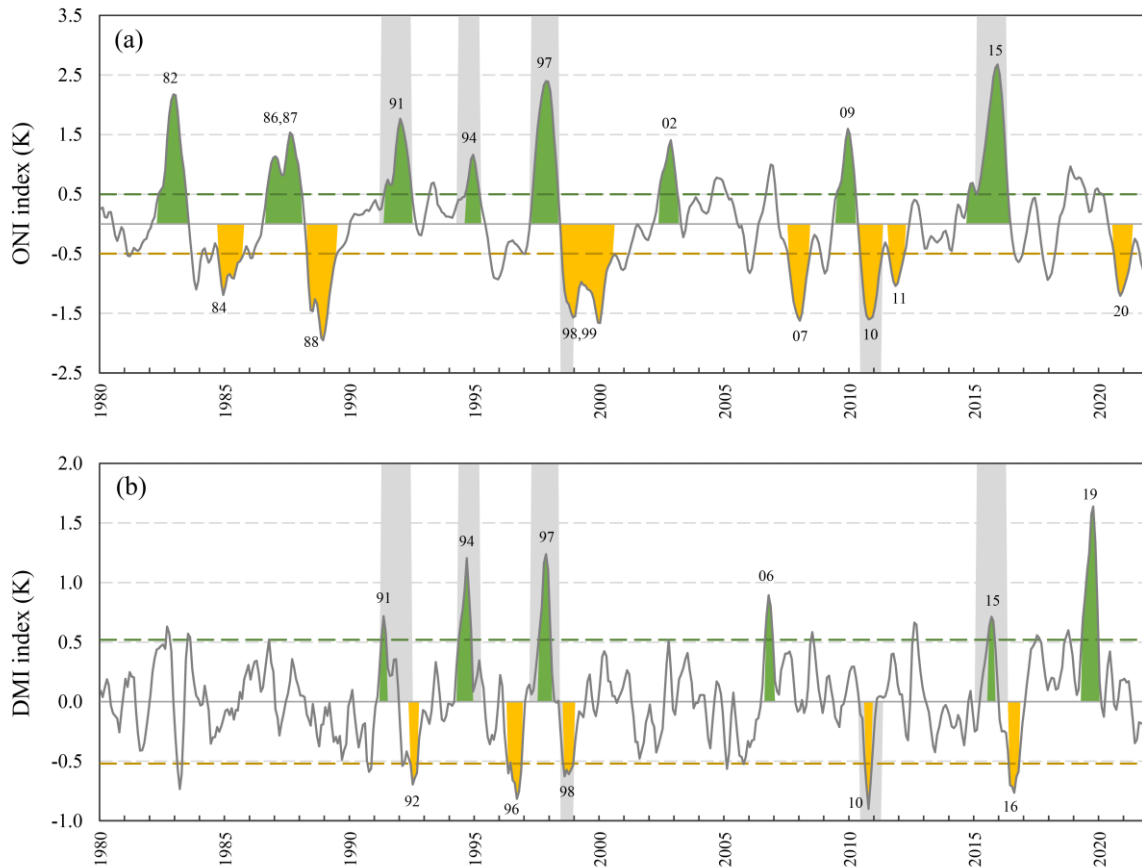
## 160 **2.3 Definition of climate events**

161 The Oceanic Niño Index (ONI) is used to define ENSO events (Fig. 1a), which represents the  
162 3-month running mean SST anomaly in the Niño 3.4 region ( $5^\circ\text{N}$ - $5^\circ\text{S}$ ,  $120^\circ$ - $170^\circ\text{W}$ ). The  
163 positive phase of an ENSO event (El Niño) is characterized by the ONI exceeding  $+0.5\text{K}$  for  
164 five consecutive overlapping 3-month periods. Conversely, the negative phase of an ENSO  
165 event (La Niña) occurs when the ONI is below  $-0.5\text{K}$  for five consecutive overlapping 3-month  
166 periods. The severity of the event can be further categorized into weak ( $0.5\sim-0.99$ ), moderate  
167 ( $1.00\sim-1.49$ ), strong ( $1.50\sim-1.99$ ) and extremely strong ( $\geq 2.00$ ) based on the absolute value  
168 of the ONI. To qualify for a specific rating, an event should meet or exceed a threshold for at  
169 least three consecutive overlapping three-month periods.

170

171 Moreover, the Dipole Mode Index (DMI) is employed to identify IOD events (Saji et al., 1999).  
172 The DMI is calculated from SST differences between the Western Equatorial Indian Ocean  
173 ( $10^\circ\text{S}$ - $10^\circ\text{N}$ ,  $50^\circ$ - $70^\circ\text{E}$ ) and the South-eastern Equatorial Indian Ocean ( $10^\circ\text{S}$ - $0^\circ\text{N}$ ,  $90^\circ$ - $110^\circ\text{E}$ )  
174 (Fig.1b). Given that the short duration of IOD events with a tendency to peak during the SON,  
175 the standard deviation of SON DMI ( $0.52\text{K}$  from 1981 to 2021) is used as the criterion for

176 identifying IOD events. A positive phase IOD (pIOD) event is defined when the absolute value  
 177 of DMI is greater than or equal to one standard deviation (0.52 K) for three consecutive 3-  
 178 month periods. Additionally, a strong pIOD event is identified if the DMI value exceeds two  
 179 standard deviations (1.04 K).



180  
 181 Fig.1 Time series of the Oceanic Niño Index (ONI) (a) and the Dipole Mode Index (DMI) (b) from 1980  
 182 to 2022. The positive phase events (El Niño and positive Indian Ocean Dipole (pIOD)) are filled in  
 183 green and the negative phase events (La Niña and negative IOD (nIOD)) are filled in yellow, and the  
 184 events are also labeled with a two-digit year. The green and yellow dashed lines represent the positive  
 185 and negative thresholds for El Niño-Southern Oscillation (ENSO) and IOD, respectively. The gray  
 186 background indicates years with the simultaneous ENSO and IOD events.

## 187 2.4 Partial correlation analysis

188 To comprehensively assess the impacts of ENSO and IOD on GPP, while accounting for the  
 189 influence of other events, partial correlation analysis (pcor) was employed, following the



190 previous studies (Saji and Yamagata, 2003; Wang et al., 2021b). The definition of  $pcor$  for  $x$   
 191 and  $y$ , controlling for  $z$ , is given by:

$$192 \quad pcor_{yx.z} = \frac{r_{yx} - r_{yz}r_{xz}}{\sqrt{1-r_{yz}^2}\sqrt{1-r_{xz}^2}} \quad (4)$$

193 where  $r_{yx}$  is the correlation of the dependent variable  $y$  and the explanatory variable  $x$  (e.g.,  
 194 DMI), and the same is for  $r_{yz}$  and  $r_{xz}$ . The two-tailed Student's  $t$ -test was used to calculate  
 195 the statistical significance of each pixel result:

$$196 \quad t = pcor_{yx.z} \sqrt{\frac{n-2-k}{1-pcor_{yx.z}^2}} \quad (5)$$

197 where  $n$  and  $k$  are the number of samples and conditioned variables, respectively.

198

## 199 **2.5 Composite analysis**

200 When enumerating the years of ENSO and IOD events, we retained all the years of IOD events  
 201 and ENSO events of above the moderate intensity. Individual events and compound events were  
 202 categorized and summarized in Table 1. In this study, a compound event refers to the  
 203 simultaneous occurrence of ENSO and IOD, primarily El Niño & pIOD and La Niña & negative  
 204 IOD (nIOD). IOD typically peaked in the September-October-November (SON, yr0), while  
 205 ENSO peaked in the December(yr0)-January(yr1)-February(yr1) (DJF), and the influence of  
 206 the two events could extend until the summer of the following year. Therefore, we selected four  
 207 seasons from SON to June-July-August (JJA) in the following year for composite analysis in  
 208 this study. In addition, the year 1991 was excluded due to the strong eruption of Mount Pinatubo,  
 209 which had a large impact on the global carbon cycle (Mercado et al., 2009).

210

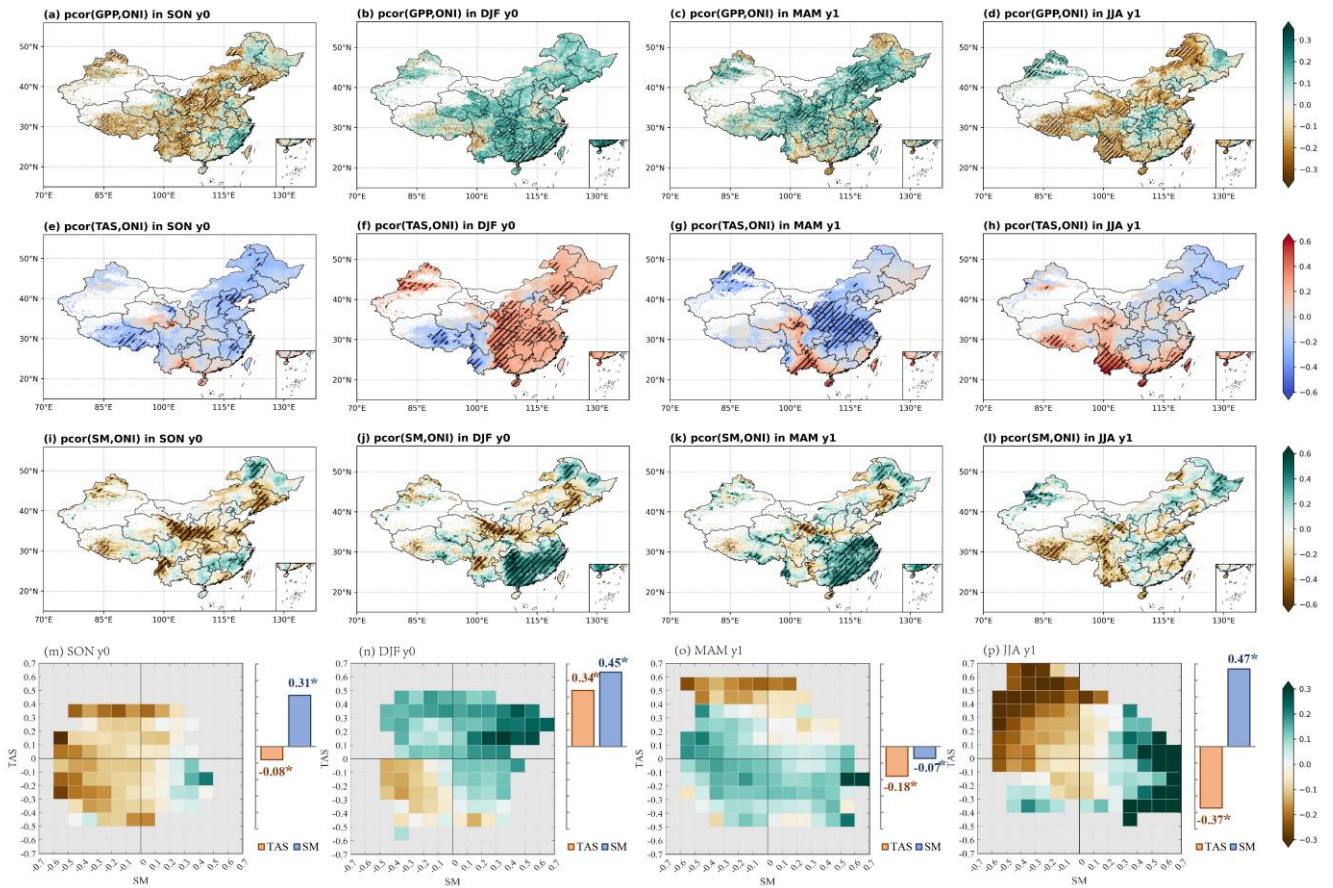
211 **Table 1.** Occurrences of ENSO and IOD events from 1981 to 2021.

| Events         | Years                              |
|----------------|------------------------------------|
| El Niño        | 1982, 1986, 1987, 2002, 2009       |
| La Niña        | 1984, 1988, 1999, 2007, 2011, 2020 |
| pIOD           | 2019                               |
| nIOD           | 1992, 1996, 2016                   |
| El Niño & pIOD | 1994, 1997, 2015                   |
| El Niño & nIOD | -                                  |
| La Niña & pIOD | -                                  |
| La Niña & nIOD | 1998, 2010                         |

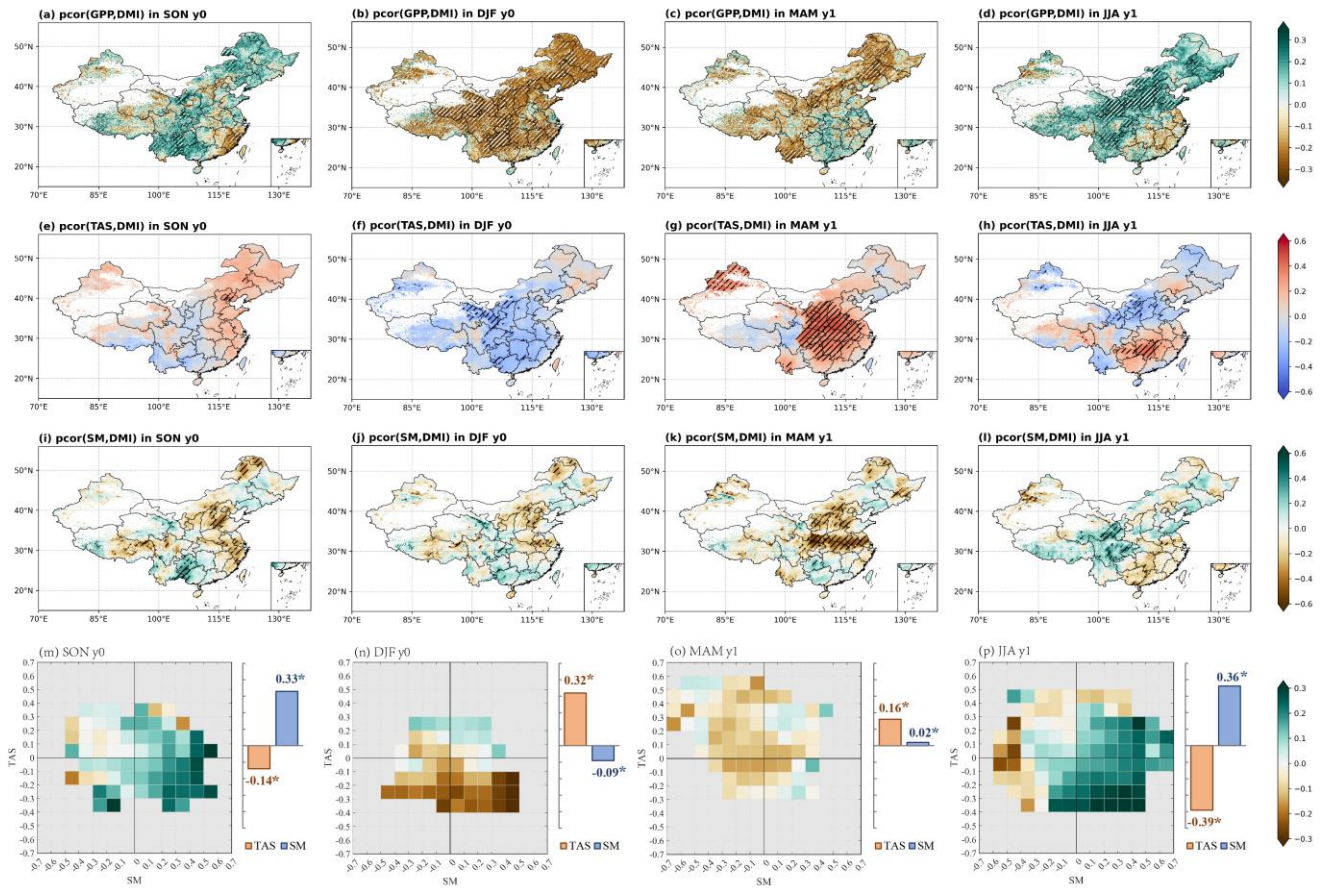
212

213 **3.Results**

214 **3.1 Historical relationship between GPP and ENSO**



215  
 216 Fig. 2 Spatial patterns of partial correlation coefficients (*pcor*) between ONI and gross primary productivity  
 217 (GPP) (a-d), surface air temperature (TAS) (e-h), soil moisture (SM) (i-l) in different seasons, controlling  
 218 for the effect of DMI. Hatched areas represent significance at  $p \leq 0.05$  based on the two-tailed Student's *t*-  
 219 test. (m-p) Heatmaps represent the relationships of the *pcor* patterns among GPP, TAS, and SM, and bar  
 220 charts illustrate the pattern correlations of these *pcor* values between GPP and TAS and SM on the national  
 221 scale for each season. We here use seasonal average temperature as a mask to exclude regions with  
 222 temperatures below zero, thereby minimizing the influence of phenology on GPP. Notably, asterisks (\*) in  
 223 the bar charts denote significance at  $p < 0.05$ .



224

225 Fig. 3 Same as Fig.2, but for DMI, controlling the effect of ONI.

226

227 We analyzed the *pcor* patterns between GPP and climate anomalies across different events  
 228 using long time series data (Figs. 2 and 3). Following this, we calculated pattern correlation  
 229 coefficients between the GPP and climate *pcor* patterns, aiming to investigate the varying  
 230 impacts of key climate drivers (TAS and SM) on photosynthesis across different seasons (Figs.  
 231 2m-p, and 3m-p).

232

233 Figure 2 reveals notable seasonal variations in the *pcor* patterns between GPP, related climate  
 234 anomalies, and ONI index in December-January-February (DJF) when ENSO peaked,  
 235 controlling the effect of DMI in September-October-November (SON) when IOD peaked.  
 236 During SON, significant negative *pcor* between GPP and ONI is observed in regions including  
 237 the Tibetan Plateau, Southwestern China, Loess Plateau, and Liaoning province (Fig. 2a).  
 238 Clearly, this pattern aligns closely with the *pcor* pattern between soil moisture and ONI (Figs.

239 2a and i). The pattern correlation analysis between GPP and both TAS and SM underscores the  
240 dominance of SM in influencing GPP anomalies, indicated by a correlation coefficient of 0.31  
241 ( $p < 0.05$ ). This finding suggests that the soil moisture deficit induced by El Niño largely  
242 inhibits vegetation photosynthesis during this season (Fig. 2m).

243

244 Along with the peak of ENSO events in DJF, the *pcor* pattern between GPP and ONI exhibits  
245 a distinct shift from the pattern in SON. Notably, DJF showcases significant positive *pcor*  
246 values over large areas in southern China and weak positive *pcor* in the North and Northeastern  
247 China (Fig. 2b). During this period, soil moisture still serves as a more influential factor in  
248 driving GPP changes, reflected in a nation-wide pattern correlation coefficient of 0.45 ( $p < 0.05$ )  
249 (Fig. 2n). Specifically, sufficient soil moisture during El Niño, coupled with higher winter  
250 temperatures, contribute to a substantial enhancement in GPP across Southern China. In  
251 contrast, the impact is weaker in the North and Northeast China due to the vegetation being in  
252 the non-growing season, and localized soil water deficits (Figs. 2b, f, and j). In addition, GPP  
253 experiences inhibition in some areas of southwestern China due to low temperatures and soil  
254 drought.

255

256 Subsequently, the positive *pcor* of GPP decreases, or even turns slightly negative from DJF to  
257 March-April-May (MAM) in southern China, primarily attributed to shifts of temperature (Figs.  
258 2c and g). On a nationwide scale, temperature becomes the dominant factor in this period, but  
259 it exhibits a negative correlation with GPP, with a spatial correlation coefficient of  $-0.18$  ( $p <$   
260  $0.5$ ). This negative correlation is mainly due to negative GPP and positive temperature in the  
261 southwest region, and positive GPP and negative temperature in the northern region (Figs. 2c  
262 and 2g). Specifically, the negative *pcor* of GPP in southwest China is due to soil moisture  
263 shortages (Fig. 2k). In the northern region, where a large area of croplands exists (Fig. S11),  
264 human management practices may have a greater impact on GPP, particularly in the spring  
265 when the growing season begins. However, these human management practices (e.g., irrigation,  
266 fertilization, pesticide use) are not considered in the BEPS model, which could introduce

267 significant uncertainties in simulated GPP over cropland areas. Additionally, in some  
268 grasslands of northern Hebei and parts of neighboring Inner Mongolia, GPP shows positive  
269 *pcor* during El Niño events, possibly due to the strong legacy effects of climatic conditions in  
270 DJF period.

271

272 Moving into JJA, the *pcor* of GPP exhibits widespread negative values again (Fig. 2d). In  
273 general, during El Niño, increased soil moisture and lower temperatures greatly contribute to  
274 enhanced GPP, while drier soil moisture and higher temperatures inhibit the increase in GPP  
275 (Fig. 2p). Regionally, higher temperatures and lower soil moisture both contribute to the  
276 negative GPP anomalies over southwestern China. However, lower soil moisture  
277 predominantly curtails GPP over the Tibetan Plateau, the Yellow River basin, and northeastern  
278 Inner Mongolia. Overall, the correlation coefficients between GPP and TAS and SM in summer  
279 are comparable, with soil moisture exhibiting a slightly higher effect, represented by a  
280 correlation coefficient of 0.47 ( $p < 0.05$ ), compared to a correlation coefficient of  $-0.37$  ( $p <$   
281  $0.05$ ) for temperature.

282

### 283 **3.2 Historical relationship between GPP and IOD**

284 In comparison, the *pcor* patterns between GPP and DMI in SON, controlling for the effect of  
285 ONI, exhibit nearly opposite patterns to those between GPP and ONI (Figs. 2 and 3). In detail,  
286 GPP demonstrates significant positive *pcor* values with DMI in southwestern China and eastern  
287 Inner Mongolia, but displays significant negative *pcor* with DMI in southeastern China during  
288 SON (Fig. 3a). In terms of climate drivers, during the pIOD events, for instance, wetter soil  
289 and lower temperatures both benefit the significant enhancement in GPP in southwestern China,  
290 while higher temperatures largely contribute to the enhancement in GPP over eastern Inner  
291 Mongolia. Conversely, GPP is largely inhibited by the dry conditions in southeastern China  
292 (Figs. 3e and i). Overall, soil moisture dominates the GPP anomaly in China, with a correlation  
293 coefficient of 0.33 ( $p < 0.05$ ) (Fig. 3m).

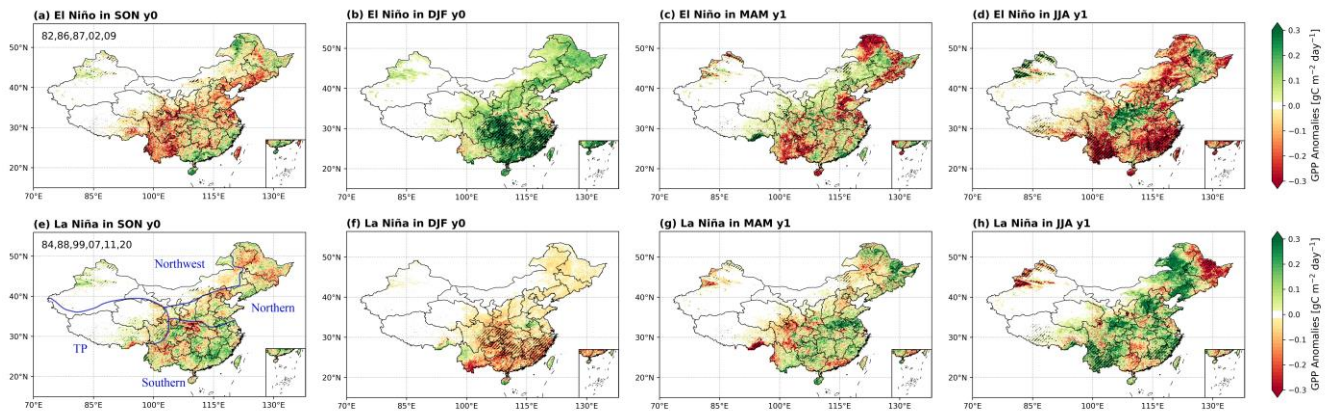
294 In DJF, GPP exhibits widespread significant negative *pcor* with DMI (Fig. 3b), primarily due  
295 to the widespread negative *pcor* of temperature, characterized by a correlation coefficient of  
296 0.32 ( $p < 0.05$ ) (Figs. 3f and n). Moving into MAM, the significant negative *pcor* between GPP  
297 and DMI carried on from those in DJF, but shifts to weak positive *pcor* in southeastern China,  
298 driven by the significant positive *pcor* of temperature (Figs. 3c and g). However, the significant  
299 negative *pcor* of soil moisture in the Jianghuai Basin and North China still negates the positive  
300 effect of temperature (Fig. 3k). During this period, temperature remains the dominant factor,  
301 with a nation-wide pattern correlation coefficient of 0.16 ( $p < 0.05$ ) with GPP (Fig. 3o).

302

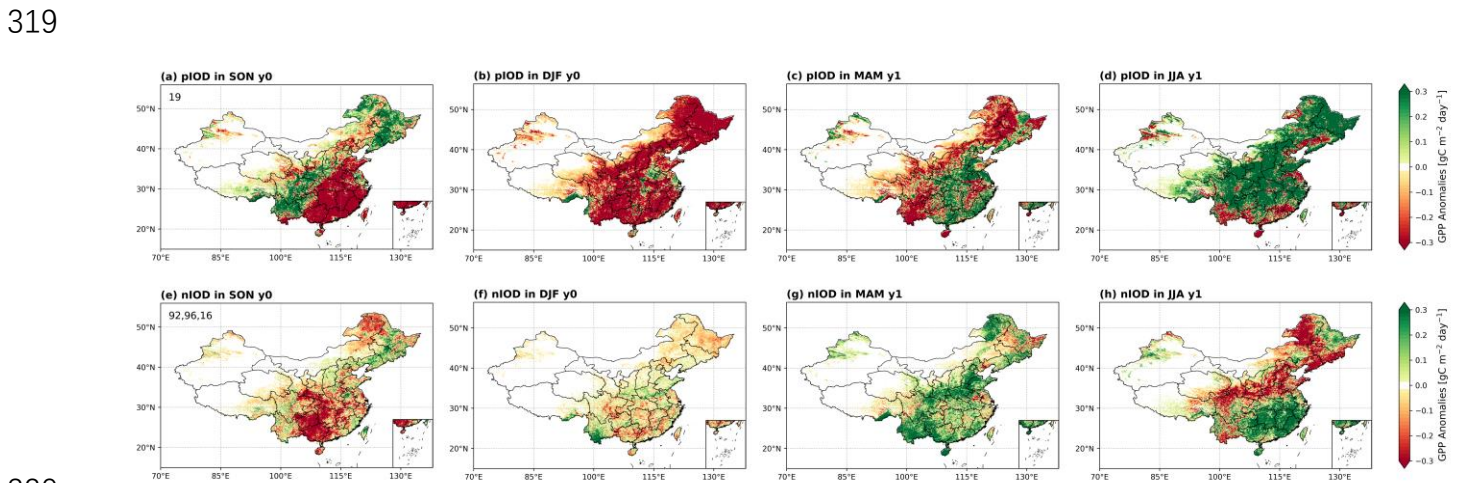
303 In JJA, the situation undergoes a change, showing the significant positive *pcor* of GPP over  
304 southwestern, north and northeast China, and weak negative *pcor* over southeastern China (Fig.  
305 3d). In other words, lower temperatures and gradually wetter soil are conducive to the increase  
306 in vegetation photosynthesis, but heat and dry conditions cause the weak inhibition of  
307 photosynthesis in southeastern China during the pIOD (Figs. 3p). However, unlike the ENSO  
308 event, the role of temperature is slightly higher than that of SM in the IOD event, and the  
309 correlations between GPP and TAS and SM are  $-0.39$  and  $0.36$  ( $p < 0.05$ ), respectively.

310

311 **3.3 GPP anomalies caused by specific ENSO and IOD events**



312  
 313 Fig. 4. Spatial distributions of seasonal composite GPP anomalies for ENSO events, (a-d) for El Niño,  
 314 and (e-h) for La Niña. The black slashes indicate areas where El Niño events differ significantly from  
 315 La Niña events ( $p \leq 0.05$ ) based on the Student's two-sample  $t$ -test. The two-digit year in first column  
 316 denote the years used for composite analysis. Additionally, China is divided into four regions:  
 317 Northwest China, Tibetan Plateau, Northern China, and Southern China, as shown in (e), which is used  
 318 in the following context.



320  
 321 Fig. 5. Similar to Fig. 4, but for spatial distributions of seasonal composite GPP anomalies for IOD  
 322 events, (a-d) for pIOD, and (e-h) for nIOD. We did not conduct the significance test here owing to the  
 323 limited samples.

324



325 While we have elucidated the historical relationship between GPP and ENSO and IOD events  
326 through partial correlation coefficients and discussed the underlying climate drivers, we here  
327 specifically selected actual events to conduct a composite analysis. This approach aims to  
328 further comprehensive understanding of the effects of ENSO and IOD events on GPP variations  
329 in China.

330

### 331 **3.3.1 ENSO-induced GPP anomalous patterns**

332 The impacts of El Niño and La Niña events exhibit opposite influences on GPP with obvious  
333 seasonal variations (Fig. 4). Specifically, during SON, GPP anomalies are relatively weak,  
334 indicating some suppressions over southwestern China and north China during El Niño events,  
335 primarily attributed to dry conditions there (Figs. 4a and S4a). As ENSO peaks in DJF, GPP is  
336 significantly strengthened during El Niño events and suppressed during La Niña events,  
337 especially over southern China (Figs. 4b and f), aligning well with the patterns of *pcor* between  
338 GPP and ONI, controlling the effect of DMI (Fig. 2b). Concurrently, the widespread higher  
339 temperatures and wetter soil moisture both contribute to enhanced GPP over southern China  
340 during El Niño events (Figs. S3b and S4b), while colder temperatures and drier soil moisture  
341 lead to GPP suppression there during La Niña (Figs. 2f and 3f). In MAM as ENSO weakens  
342 and vegetation starts to grow in the extratropics, the enhanced GPP over southern China in DJF  
343 during El Niño events diminishes, even transitioning into a notable GPP reduction over  
344 southwestern China, north China, and northeastern China (Fig. 4c). This transition is conspired  
345 by phenological and climate changes including colder temperatures and prolonged dry  
346 conditions (Figs. S3c and S4c). The GPP pattern exhibits the opposite transition in La Niña  
347 (Fig. 4g). Moving to JJA, dry and hot conditions (Fig. S3d and S4d) lead to significant negative  
348 GPP anomalies in southeastern and southwestern China in El Niño (Fig. 4d), whereas cool and  
349 wet conditions result in positive GPP anomalies in La Niña events (Fig. 4h). Overall, GPP  
350 anomalies induced by ENSO events in DJF and JJA are more pronounced than those in SON  
351 and MAM, corresponding to the life cycle of event and vegetation growth periods, respectively.

352 Crucially, they demonstrate distinct GPP patterns, with significant enhancements in DJF and  
353 reductions in JJA during El Niño events and reverse during La Niña events, aligning well with  
354 the *pcor* pattern between GPP and ONI, controlling for the effect of DMI (Fig. 4). In addition,  
355 the effect of ENSO on vegetation in southern China appears more substantial.

356

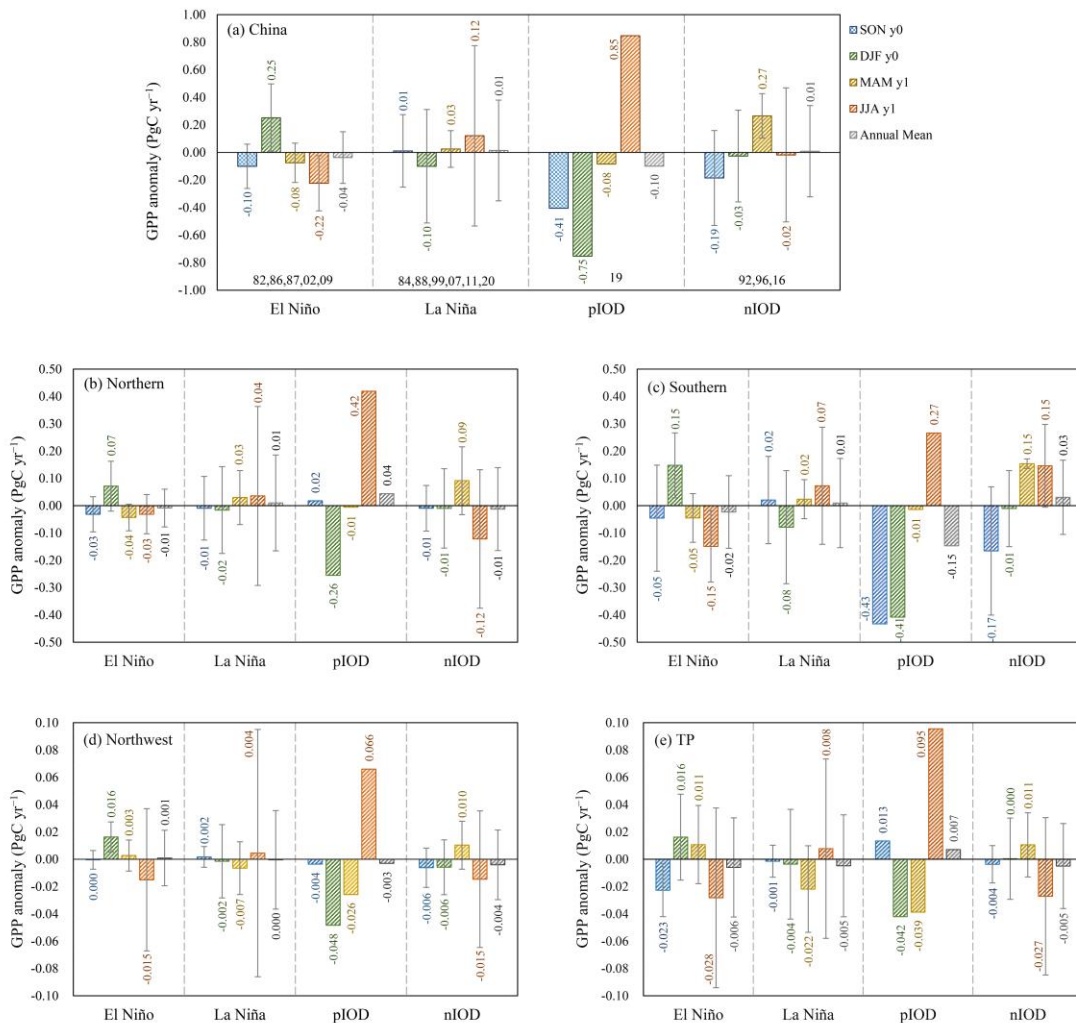
### 357 **3.3.2 IOD-induced GPP anomalous patterns**

358 During the period from 1981 to 2021, we only find one independent but extreme pIOD event  
359 occurred in 2019 according to our criterion (Table 1). This extreme pIOD event extended from  
360 June to December, a longer duration compared to other IOD events. Different from ENSO,  
361 IOD basically peaks in SON. GPP anomalies induced by this extreme event align closely with  
362 the long-term *pcor* patterns between GPP and DMI, controlling for the effect of ONI (Fig. 3).  
363 Specifically, significant reductions in GPP occur in southeastern China in SON (Fig. 5a),  
364 predominantly due to heat stress and severe drought conditions (Figs. S5a and S6a), consistent  
365 with the findings revealed by Wang et al. (2021b). In DJF, the seasonal legacy of vegetation  
366 state (Yan et al., 2023) and prolonged droughts lead to the widespread GPP reductions (Figs.  
367 5b and S6b), outweighing the potential positive effect of higher temperatures (Fig. S5b). Of  
368 course, the decline of GPP in southwestern China appears linked to lower temperatures (Figs.  
369 5b and S5b). During MAM, the mitigation of soil moisture deficit and favorable higher  
370 temperatures in southern China facilitate a shift in GPP from decline to increase (Fig. 5c). In  
371 the north, persistent drought conditions notwithstanding (Fig. S6c), higher temperatures and  
372 the onset of the growing season contribute to the enhanced GPP (Fig. 5c). In JJA, increased  
373 precipitation over the Yangtze and Yellow River basins (Zhang et al., 2022) alleviates the soil  
374 moisture deficits (Fig. S6d). Coupled with the relatively lower temperatures, this leads to  
375 widespread GPP increases. Conversely, GPP suppressions in provinces south of 25°N and  
376 around the Bohai Sea are attributed to higher temperatures and soil water deficits (Figs. 5d,  
377 S5d, and S6d).

378

379 In contrast to the intense 2019 pIOD event, our composite analysis incorporates three weak  
380 nIOD events, resulting in comparatively milder anomalies. In SON, different from pIOD event,  
381 negative GPP anomalies in nIOD mainly appear in the provinces of Guizhou, Hunan, and  
382 Guangxi (Fig. 5e), associated well with concurrent dry conditions (Fig. S6e). In DJF, although  
383 the spatial pattern of soil moisture remains largely consistent with SON (Fig. S6f), a shift from  
384 negative to positive temperature anomalies mitigates the evident GPP reductions (Fig. 5f). The  
385 ongoing soil wetting and the onset of the growing season in northern hemisphere in MAM  
386 result in the increased GPP over the Yellow River Basin and southwestern China (Figs. 5g, S5g,  
387 and S6g). Subsequently, in JJA, the combination of wetter soil and lower temperatures  
388 facilitates vegetation photosynthesis in southern China, while drier soil largely contributes to  
389 the reduction in GPP in the north and northeastern China (Figs. 5h, S5h, and S6h).  
390

391 **3.3.3 National and regional total GPP anomalies**



392  
 393 Fig. 6. The seasonal and annual mean anomaly of GPP in different classified events for China (a), for  
 394 Northern China (b), for Southern China (c), for Northwest China (d), and for Tibetan Plateau (e). The  
 395 error bars show the standard deviation of different events in the composite analysis.

396  
 397 We calculated the total GPP anomaly in China and various geographic regions for each  
 398 classified event on both seasonal and annual scales (Fig. 6). Regionally, the geographical  
 399 divisions include Northern China, Southern China, Northwest China, and Tibetan Plateau (Fig.  
 400 4e). Notably, the North-South boundary aligns closely with the 0° isotherm in January and the  
 401 annual precipitation line of 800 mm. The division between the North and the Northwest is

402 determined by the annual precipitation line of 400 mm, and the Tibetan Plateau is segmented  
403 based on topographic factors.

404

405 In general, the GPP anomalies exhibit noticeable differences on the seasonal scale, while the  
406 total annual anomalies do not show a significant magnitude due to the mutual offset of positive  
407 and negative anomalies in different seasons. However, it is worth noting that our annual totals  
408 are calculated from the SON in the developing year of the event to the JJA in the following  
409 year. This method deviates from the traditional calendar year, and as per the conventional  
410 definition of a “year”, the annual anomalies induced by these events can indeed be substantial.

411

412 Specifically, taking a national perspective (Fig. 6a), GPP anomalies during the El Niño and La  
413 Niña events exhibit opposite signs in DJF and JJA, with greater magnitudes during these peak  
414 periods of the events and the most vigorous growth period of vegetation, respectively. In terms  
415 of the development process of the event, the annual anomaly of GPP is negative during El Niño,  
416 with a magnitude of  $-0.04 \pm 0.19 \text{ Pg C yr}^{-1}$ , but positive during La Niña events, with a  
417 magnitude of  $0.01 \pm 0.37 \text{ Pg C yr}^{-1}$ . The asymmetry of the positive and negative phases of IOD  
418 is also evident in the total anomaly. For the pIOD event in 2019, GPP shows strong negative  
419 anomalies with values of  $-0.41 \text{ Pg C yr}^{-1}$  in SON and  $-0.75 \text{ Pg C yr}^{-1}$  in DJF. Conversely, it  
420 exhibits a marked positive anomaly in the following JJA, with a value of  $0.85 \text{ Pg C yr}^{-1}$ . The  
421 annual total of GPP anomaly is opposite for pIOD and nIOD events, showing  $-0.10 \text{ Pg C yr}^{-1}$   
422 and  $0.01 \pm 0.33 \text{ Pg C yr}^{-1}$ , respectively. Moreover, large standard deviation indicated that there  
423 are large uncertainties in the impact of different events, and each event has its uniqueness  
424 (Capotondi et al., 2015).

425

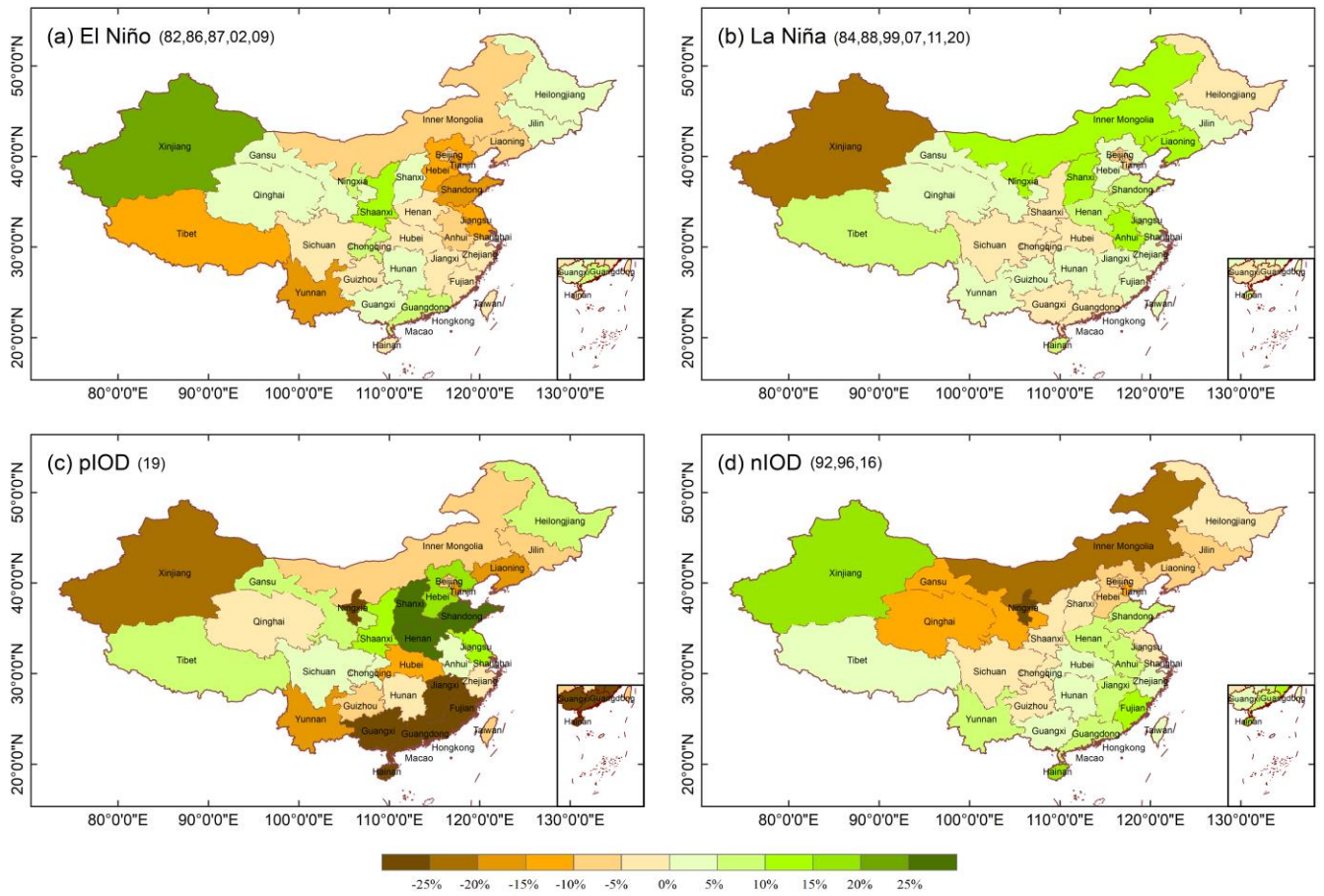
426 Additionally, the variation of GPP anomaly in each region is basically consistent with that at  
427 the national scale, especially in the Southern. But regional differences indeed exist in the total  
428 amount of GPP anomalies, demonstrating the difference in the impact of events on different  
429 regions' GPP. Taking the 2019 extreme pIOD event as an example, the GPP showed a

430 significant negative anomaly in the Southern during the SON (Fig. 6c), resulting in negative  
431 anomalies in GPP at the national scale (Fig. 6a), but weak positive anomalies in the Northern  
432 and TP (Figs. 6b and e). Then, the GPP anomaly was close to zero in the Northern and Southern  
433 in MAM (Figs. 6b and c), while it was still a significant negative anomaly in the Northwest  
434 and TP (Figs. 6d and e). Moreover, the negative annual GPP anomalies in the Southern and  
435 Northwest offset the positive anomalies of the TP and Northern, making a negative annual GPP  
436 anomaly in the national of this event.

437

438 In terms of the magnitude of GPP anomalies, they are more pronounced in the Northern and  
439 Southern regions, characterized by lush vegetation, mostly less than  $0.5 \text{ Pg C yr}^{-1}$ .  
440 Meanwhile, GPP anomalies are relatively weaker in the Northwest and TP regions, primarily  
441 covered by grassland, generally less than  $0.1 \text{ Pg C yr}^{-1}$ . Further, we calculate the contributions  
442 of different regions to the national total GPP anomaly in each event (Table S3), referencing an  
443 index described in the article by Ahlstrom et al. (2015), as detailed in the supplementary method.  
444 Overall, the GPP anomaly in the Southern region dominates the national GPP variation,  
445 contributing approximately 68% to ENSO events and 46% to IOD events, respectively. The  
446 Northern GPP anomaly contributes approximately 28% to the national GPP variation in ENSO  
447 events and 39% in IOD events. In addition, the contribution of GPP anomaly in the Northwest  
448 and TP regions to the national GPP variation is within 10%.

449 **3.3.4 Relative changes in total GPP anomalies at provincial scale**



450

451 Fig. 7. Spatial distributions of relative changes of total composite anomalies of GPP at provincial scale

452 for different classified events.

453 We presented the spatial patterns of mean GPP anomalies from the SON in the developing year  
454 to the JJA in the decaying year (Fig. S7) and further calculated provincial total GPP anomalies  
455 (Fig. S8 and Table S3). Provinces with more extensive forest coverage, such as Yunnan, central  
456 provinces housing the Qinling Mountains, and northeast provinces where the Greater and  
457 Lesser Hinggan Mountains are situated, exhibit relatively larger provincial GPP anomalies.  
458 However, differences are apparent among different events (Fig. S8). Considering differences  
459 in area and vegetation coverage across provinces, our focus centers on the relative change of  
460 GPP anomalies (Fig. 7). It's important to note that, due to different years used in composite  
461 analysis, our quantitative comparisons are limited to the same event within different provinces,  
462 while qualitative descriptions are extended to different events.

463

464 El Niño events generally induce substantial GPP changes in two main regions with a relative  
465 change of over 10% (Fig. 7a). One region encompasses the northern coastal provinces,  
466 including Tianjin, Hebei, Shandong, and Jiangsu, while the other is situated in the western part,  
467 including Xinjiang, Tibet, and Yunnan provinces. Yunnan, rich in forest resources, bears the  
468 brunt of El Niño 's impact, exhibiting a total negative GPP anomaly of  $-22.55 \text{ Tg C yr}^{-1}$  (Table  
469 S4) and a relative change of approximately 16%. Despite comparable relative changes in GPP  
470 for other provinces, their GPP anomalies are relatively smaller, within  $-5 \text{ Tg C yr}^{-1}$ . Notably,  
471 Xinjiang, characterized by a fragile forest steppe in the Altai and Tianshan Mountain regions,  
472 consistently demonstrates substantial relative changes in GPP during both ENSO and other  
473 events. Quantitatively, during the El Niño episode, Xinjiang witnesses a remarkable 24%  
474 relative change in GPP, accompanied by a positive GPP anomaly of  $-3.82 \text{ Tg C yr}^{-1}$ . In contrast,  
475 during the La Niña episode, provinces with notable relative changes are mainly concentrated  
476 in the northern regions, such as Xinjiang, Inner Mongolia, Ningxia, Shanxi, and Liaoning  
477 provinces (Fig. 7b). In addition, although the influence of ENSO on GPP in the southern China  
478 is significant (Fig. 4), the total relative change through the year remains small due to the  
479 cancellation of positive and negative anomalies in different seasons.

480 In the pIOD classification, only the 2019 extreme event is considered, resulting in the relative



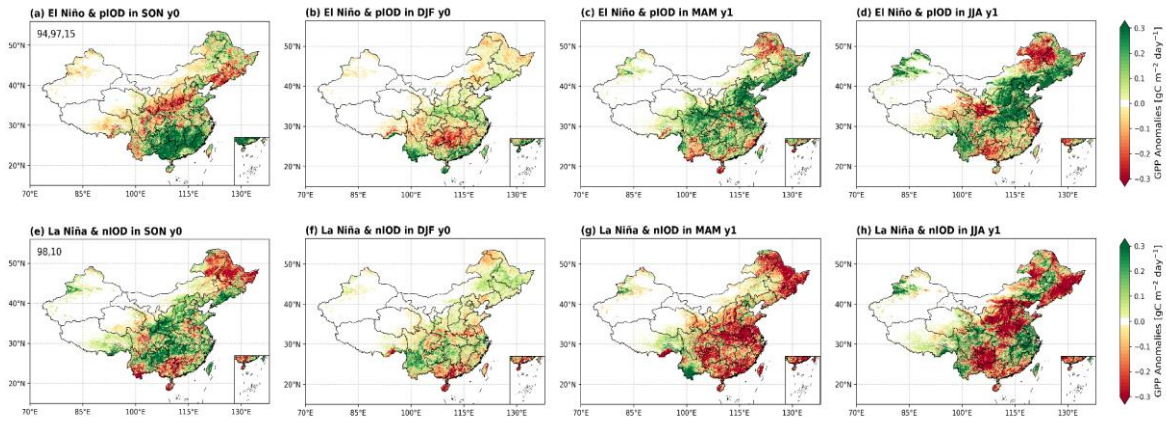
481 change in GPP anomalies exceeding 10% in approximately half of the provinces. Notably,  
482 Jiangxi, Fujian, Guangxi, Guangdong, and Hainan experience reductions of more than 25% in  
483 GPP, with Jiangxi exhibiting the largest GPP anomaly of  $-31.50 \text{ Tg C yr}^{-1}$ . Conversely,  
484 Shandong, Shanxi, and Henan witness increase of over 25% in GPP (Fig. 7c). During nIOD  
485 events, northern provinces generally exhibit negative relative changes, while southern  
486 provinces display positive relative changes.

487

488 In summary, the relative changes in total GPP anomalies at the provincial scale exhibit an east-  
489 west pattern in annual variation. Meanwhile, the influence of IOD events on GPP presents an  
490 opposing north-south pattern.

491 **4. Discussion**

492 **4.1 The effect of compound ENSO and IOD events on China's GPP**



493

494 Fig. 8. Spatial distributions of seasonal composite GPP anomalies for compound events, (a-d) for El  
495 Niño & pIOD events, and (e-h) for La Niña & nIOD events. The two-digit year in first column denote  
496 the years used for composite analysis.

497

498 Indeed, despite IOD events being generally considered an independent coupled ocean-  
499 atmosphere interaction (Saji et al., 1999), historical IOD events can occur in conjunction with  
500 ENSO (Ham et al., 2017; Yang et al., 2015). These combined phenomena are most notable  
501 represented by El Niño & pIOD and La Niña & nIOD events. Williams and Hanan (2011)  
502 researched the interactive effects of ENSO and IOD on African GPP, relying on an offline  
503 terrestrial biosphere model simulation. Their findings suggested that IOD could cause obvious  
504 anomalous GPP over much of Africa, capable of suppressing or even reversing ENSO signals  
505 in GPP anomalies. In addition, Yan et al. (2023) explored the interactive effects of ENSO and  
506 IOD on seasonal anomalies of tropical net land carbon flux using the TRENDYv9 multi-model  
507 simulations, revealing diverse effects in different sub-continent and seasons. We explore the  
508 anomalies of GPP in compound events based on composite analysis (Fig. 8), and the spatial  
509 patterns of soil moisture and temperature anomalies are shown in the appendix (Figs. S9 and  
510 S10).

511

512 The spatial patterns of the GPP anomalies during concurrent ENSO and IOD events differ from  
513 those in single events, although some similarities are evident. ~~GPP anomalies in El Niño &~~  
514 ~~pIOD and La Niña & nIOD events are generally opposite, and we focus specifically on El Niño~~  
515 ~~& pIOD events here.~~ We observed that GPP anomalies during El Niño & pIOD events are  
516 generally opposite to those during La Niña & nIOD events. Here, we focus on the impacts of  
517 El Niño & pIOD events. ~~In El Niño & pIOD events, GPP anomalies exhibit a general opposition,~~  
518 ~~with enhanced vegetation photosynthesis in the southern regions and inhibited in the northern~~  
519 ~~regions during SON.~~ During El Niño & pIOD events, photosynthesis generally increased in the  
520 southern regions and decreased in the northern regions during SON, indicating opposing GPP  
521 anomalies across these areas. This spatial characteristic of GPP anomalies bears some  
522 resemblance to that induced by El Niño alone (Figs. 4a and 8a). Weak GPP anomalies are  
523 generally observed in DJF, with noticeable negative GPP anomalies in Guizhou and Hunan,  
524 and some positive GPP anomalies in regions south of 25°N (Fig. 8b). Notably during DJF,  
525 while significant positive GPP anomalies occur in El Niño events (Fig. 4b), simultaneous pIOD  
526 events induce significant negative GPP anomalies (Fig. 5b). When both events coincide, their  
527 impacts seem to largely counterbalance each other, resulting in a more neutral GPP anomaly.  
528 In MAM, GPP increases in Northern China (Fig. 8c). Subsequently, in JJA, vegetation  
529 photosynthesis experiences a significant increase in the Northern and Yunnan provinces (Fig.  
530 8d).

531 It is worth noting that the impacts of compound events on China's GPP may not follow a  
532 straightforward linear superposition of the effects of two individual events. While their effects  
533 are nearly opposite when occurring separately, the positive and negative effects on GPP may  
534 be not simply cancelled each other out when they coincide. This complexity arises from the  
535 simultaneous occurrence of two tropical air-sea interaction modes, leading to intricate effects  
536 on mid-latitude circulations. Given the limited number of compound events, further exploration  
537 is necessary to unravel the effects of ENSO and IOD on GPP in China.

## 538 **4.2 Modulation of large-scale circulations on China's GPP**

539 China's GPP is intricately influenced by atmospheric circulations and sea surface temperature  
540 (Li et al., 2021; Ying et al., 2022). Ying et al. (2022) showed significant correlations between  
541 seasonal GPP variation in China and climate phenomena such as ENSO, Pacific Decadal  
542 Oscillation (PDO), and Arctic Oscillation (AO), based on the Residual Principal Component  
543 analysis. Their research indicated that these identified SST and circulation factors could  
544 account for 13%, 23% and 19% of the seasonal GPP variations in spring, summer and autumn,  
545 respectively. And Li et al. (2021) proved that GPP response to El Niño varied with PDO phases  
546 during the growing seasons of typical El Niño years. Although both studies emphasized the  
547 impact of ENSO on China's GPP and explored the roles of PDO and AO, the IOD was notably  
548 absent from their analyses. Contrastingly, our study sheds light on the significant influence of  
549 the extreme positive phase of IOD in 2019, showing a substantial negative GPP anomaly in  
550 southeastern China during SON, aligning with findings by Wang et al. (2021b). Moreover, the  
551 integration of partial correlation and composite analysis in our study elucidates the  
552 considerable impact of IOD on China's GPP within this context. Importantly, our research  
553 underscores the temporal and spatial variability in the effects of IOD and ENSO on GPP across  
554 different seasons and regions. This complexity in ocean-atmosphere teleconnections implies  
555 that other climate oscillations, such as Polar/Eurasia and Atlantic Multidecadal Oscillation  
556 (AMO), might also contribute to influencing China's GPP (Zhu et al., 2017).

## 557 **4.3 Uncertainties in BEPS Simulations**

558 The simulation of China's GPP by BEPS is subject to several sources of uncertainty inherent  
559 in the model's structure, parameterizations, processes, and input data (Chen et al., 2012; Chen  
560 et al., 2017; He et al., 2021a; Liu et al., 2018; Wang et al., 2021a). Leaf Area Index (LAI), a  
561 crucial input for the BEPS model, is derived from global remote sensing data that inherently  
562 possess uncertainties in spatial distribution and trend changes. Previous studies have  
563 highlighted significant uncertainties in simulating carbon budget of global terrestrial

564 ecosystems when employing different LAI remote sensing data (Chen et al., 2019; Liu et al.,  
565 2018). Foliage clumping index which is used to separate sunlit and shaded LAI can also cause  
566 some uncertainties in simulating GPP, because the current version of BEPS used the time-  
567 invariant satellite-derived clumping index (Chen et al., 2012). Biases in meteorological drivers,  
568 such as precipitation, can further result in considerable uncertainties in simulating terrestrial  
569 carbon cycle. The choice of precipitation products, for instance, has been shown to yield  
570 considerable differences in simulated net land-atmosphere carbon flux (Wang et al., 2021c).  
571 Moreover, BEPS model, like other terrestrial biosphere models, lacks consideration for  
572 vegetation adaptability to rising CO<sub>2</sub> concentration, potentially leading to an overestimation of  
573 the fertilization effect on GPP. In addition, the accuracy of simulations over agricultural areas  
574 is compromised in BEPS, as it only considers crops with a C3 photosynthetic pathway and  
575 overlooks C4 crops (He et al., 2017; He et al., 2021b; Ju et al., 2006). Although BEPS simulated  
576 GPP demonstrates relatively high consistency with the measured GPP of Yingke Station (CRO),  
577 located in the northwest of China, its accuracy lacks validation over the extensive farmlands in  
578 north and northeastern China where various crops are grown (Fig. S11). Agricultural operations,  
579 particularly irrigation, which can significantly impact GPP, are not considered in BEPS. He et  
580 al. (2021a) revealed extensive wetting signals over croplands in arid and semi-arid areas which  
581 exerted strong impacts on GPP and evapotranspiration simulations in BEPS after assimilating  
582 the Soil Moisture Active Passive (SMAP) soil moisture product. Furthermore, photosynthetic  
583 key parameters, such as carboxylation capacity at 25°C ( $V_{\text{cmax},25}$ ), can largely determine the  
584 performance in simulating GPP. After assimilating the solar-induced chlorophyll fluorescence  
585 (SIF) from the Orbiting Carbon Observing Satellite-2 (OCO-2) to optimize  $V_{\text{cmax},25}$  of different  
586 plant functional types (PFTs) in BEPS, previous studies suggested the improvements in  
587 simulating GPP at regional and global scales to some extent (He et al., 2019; Wang et al.,  
588 2021a).

589 ~~4.1 Seasonal legacy effects~~ **4.4 Limitations and Future work**

590 While the seasonal legacy effects of climate on subsequent vegetation have been widely

591 confirmed (Bastos et al., 2020; Bastos et al., 2021), they were not fully accounted for in this  
592 study. During ENSO and IOD events, temperature and soil moisture vary with seasons,  
593 resulting in diverse conditions such as high temperature and drought, high temperature and wet,  
594 low temperature and drought, and low temperature and wet across different regions and seasons.  
595 Vegetation does not immediately respond to changes in climatic condition changes due to its  
596 environmental resistance and self-regulation. These legacy effects are complex and vary by  
597 region as ENSO or IOD events progress through different seasons.

598 Spring serves as a transitional period between the peak of the climatic event and the peak of  
599 the growing season, making it challenging to fully explain the spatial patterns of GPP anomalies  
600 in parts of northern China based on temperature and soil moisture. Higher temperatures during  
601 DJF in El Niño events (Fig. 2f) can advance the growing season, subsequently impacting  
602 vegetation in the following spring. Sanders-DeMott et al. (2020) have proved that a warm  
603 winter can enhance the photosynthetic capacity of vegetation in the subsequent spring.  
604 Additionally, Yan et al. (2023) quantified the influence of the preceding and contemporaneous  
605 climatic conditions on NEP during the 1997/98 El Niño and pIOD compound event, showing  
606 that legacy effects can counteract or even reverse the effects of contemporaneous climatic  
607 conditions.

608

609 Additionally, Temperature and water (precipitation or soil moisture) have long been regarded  
610 as the main climate factors driving inter-annual fluctuations of GPP or NEP (Zeng et al., 2005;  
611 Piao et al., 2013; Ahlstrom et al., 2015; Wang et al., 2016; Jung et al., 2017; Humphrey et al.,  
612 2018). However, other factors, such as VPD and radiation, also play important roles. This may  
613 explain the occasional mismatch between GPP patterns and TAS/SM in certain regions in Figs.  
614 2 and 3. Overall, although the dominant driving factors vary seasonally, TAS and SM capture  
615 GPP variations more effectively on a national scale.

616 Finally, it is worth noting that climate factors often interact closely with one another. For  
617 example, soil moisture can influence changes in surface air temperature, and vice versa. As a  
618 result, in addition to direct effects, climate drivers may also impact vegetation through indirect

619 pathways. Humphrey et al. (2021) discussed the direct and indirect effects of soil moisture on  
620 variations in terrestrial interannual carbon sinks—specifically, through its influence on  
621 temperature and vapor pressure deficit (VPD)—using simulations from four Earth System  
622 Models. This area of interaction warrants further investigation in future research.

## 623 **5. Conclusion**

624 In this paper, we used partial correlation coefficients and composite analysis to investigate the  
625 impacts of ENSO and IOD events on China's GPP during 1981–2021. The partial correlation  
626 results reveal that the effects of ENSO and IOD on GPP and related climate in China exhibit  
627 distinct seasonal variations and are basically opposite. Specifically, during SON, significant  
628 negative *pcor* between GPP and ENSO is observed over the Tibetan Plateau, southwestern  
629 China, Loess Plateau, and Liaoning. In DJF, strongly positive *pcor* occurs over southern China,  
630 weakening in the subsequent MAM, albeit with some enhancements in northern Hebei and  
631 neighboring Inner Mongolia. The *pcor* then turns generally negative in JJA. In contrast,  
632 significant positive *pcor* between GPP and IOD is noted in southwestern and Northeast China  
633 during SON. Subsequently, widespread negative *pcor* appears during DJF, persisting  
634 significantly in most western and northern regions during MAM. In JJA, the *pcor* becomes  
635 significantly positive in southwestern, north and northeast China. Moreover, the correlation  
636 coefficients between GPP and climate show that GPP anomalies are primarily dominated by  
637 SM during ENSO events except MAM, while temperature generally plays a more important  
638 role during IOD events except SON.

639  
640 The composite analysis results validate the patterns of GPP anomalies observed in the partial  
641 correlation. Generally, China's annual total GPP demonstrates modest positive anomalies in La  
642 Niña and nIOD years, contrasting with minor negative anomalies in El Niño and pIOD years.  
643 This results from the counterbalancing effects, with significantly greater GPP anomalous  
644 magnitudes in DJF and JJA. Regionally, GPP anomalies fluctuate more in the Southern and  
645 Northern regions. The GPP anomaly in the Southern region dominates the national GPP

646 variation, with the contribution of 68% to ENSO events and 46% to IOD events, respectively.  
647 On the provincial scale, western and northern provinces in experience larger relative annual  
648 variations during ENSO events, with magnitudes exceeding 10%, exhibiting a general east-  
649 west pattern. Conversely, provinces in the southern and Northern China witness larger relative  
650 changes during IOD events, showing an opposing north-south pattern. For instance, the 2019  
651 extreme pIOD led to relative changes of over 25% in certain provinces in the south and north.  
652



653 **Author contributions**

654 Jun Wang designed the experiments. Ran Yan processed the data, carried out the analysis and wrote the  
655 original manuscript. All the authors contributed to the writing of the paper.

656 **Acknowledgement**

657 The calculations in this paper have been done on the computing facilities in the High Performance  
658 Computing Center (HPCC) of Nanjing University. This study was supported by the Natural Science  
659 Foundation of China (Grants 42141005 and 42475129), and the Natural Science Foundation of Jiangsu  
660 Province, China (BK20221449).

661 **Conflict of Interest**

662 The authors declare no competing interests.

663 **Data Availability**

664 ERA5 meteorological data are available at <https://cds.climate.copernicus.eu/cdsapp#!/dataset/reanalysis-era5-single-levels?tab=overview>. The remote-sensing GLOBMAP LAI data is available at  
665 <https://zenodo.org/record/4700264#.YzvSYnZBxD8/>. The carbon dioxide emissions data is available  
666 at [https://gml.noaa.gov/webdata/ccgg/trends/co2/co2\\_mm\\_mlo.txt](https://gml.noaa.gov/webdata/ccgg/trends/co2/co2_mm_mlo.txt). Vegetation type data for B  
667 EPS simulations is obtained from <https://lpdaac.usgs.gov/products/mcd12q1v006/>. Soil texture data  
668 is available at <https://data.tpdc.ac.cn/zh-hans/data/611f7d50-b419-4d14-b4dd-4a944b141175>. Soil  
669 moisture and surface air temperature from ERA5-Land are available at <https://cds.climate.copernicus.eu/cdsapp#!/dataset/reanalysis-era5-land-monthly-means?tab=overview>. Sea surface temperature  
670 dataset from ERSSTv5 is available at <https://psl.noaa.gov/data/gridded/data.noaa.ersst.v5.html>. Eight sites of the ten are from ChinaFlux (<http://www.chinaflux.org/enn/index.aspx>), and  
671 <https://psl.noaa.gov/data/gridded/data.noaa.ersst.v5.html>. Eight sites of the ten are from ChinaFlux (<http://www.chinaflux.org/enn/index.aspx>), and  
672 <https://psl.noaa.gov/data/gridded/data.noaa.ersst.v5.html>. Eight sites of the ten are from ChinaFlux (<http://www.chinaflux.org/enn/index.aspx>), and  
673 <https://psl.noaa.gov/data/gridded/data.noaa.ersst.v5.html>.

674 two are from National Tibetan Plateau Third Pole Environment (<http://data.tpdc.ac.cn/zh-hans>).  
675 FluxSat GPP Version 2.2 are available at [https://avdc.gsfc.nasa.gov/pub/tmp/FluxSat\\_GPP](https://avdc.gsfc.nasa.gov/pub/tmp/FluxSat_GPP).

676

## 677 **Reference**

678 Ahlstrom, A., Raupach, M. R., Schurgers, G., Smith, B., Arneeth, A., Jung, M., Reichstein, M., Canadell,  
679 J. G., Friedlingstein, P., Jain, A. K., Kato, E., Poulter, B., Sitch, S., Stocker, B. D., Viovy, N., Wang,  
680 Y. P., Wiltshire, A., Zaehle, S., Zeng, N.: The dominant role of semi-arid ecosystems in the trend and  
681 variability of the land CO<sub>2</sub> sink, *Science*, 348(6237), 895-899, <https://doi:10.1126/science.aaa1668>,  
682 2015.

683 Antonietta, C., Andrew, T., Matthew, N., Emanuele, Di., Jin-Yi, Y., Pascale, B., Julia, C., Boris, D.,  
684 Benjamin G., Eric, G., Fei-Fe, J., Kristopher, K., Benjamin, K., Tong, L., Niklas, S., Yan, X., and Sang-  
685 Wook, Y.: Understanding ENSO Diversity, *B. Am. Meteorol. Soc.*, 96(6), 921-938,  
686 <https://doi:10.1175/BAMS-D-13-00117.1>, 2015.

687 Bastos, A., Ciais, P., Friedlingstein, P., Sitch, S. and Zaehle, S.: Direct and seasonal legacy effects of  
688 the 2018 heat wave and drought on European ecosystem productivity. *Sci. Adv.*, 6, eaba2724,  
689 <https://doi.org/10.1126/sciadv.aba2724>, 2020.

690 Bastos, A., Orth, R., Reichstein, M., Ciais, P., Viovy, N., Zaehle, S., Anthoni, P., Arneeth, A., Gentine, P.,  
691 Joetzjer, E., Lienert, S., Loughran, T., McGuire, P. C., O, S., Pongratz, J., and Sitch, S.: Vulnerability of  
692 European ecosystems to two compound dry and hot summers in 2018 and 2019, *Earth Syst. Dynam.*,  
693 12, 1015–1035, <https://doi.org/10.5194/esd-12-1015-2021>, 2021.

694 Bauch, M.: Chapter 15 - Impacts of extreme events on medieval societies: Insights from climate history,  
695 in: *Climate Extremes and Their Implications for Impact and Risk Assessment*, edited by: Sillmann, J.,  
696 Sippel, S., and Russo, S., Elsevier, 279-291, <https://doi.org/10.1016/B978-0-12-814895-2.00015-X>,  
697 2020.

698 Chen, J., Liu, J., Cihlar, J., and Goulden, M.: Daily canopy photosynthesis model through temporal and  
699 spatial scaling for remote sensing applications, *Ecol. Model.*, 124, 99–119, [https://doi:10.1016/S0304-](https://doi:10.1016/S0304-3800(99)00156-8)  
700 [3800\(99\)00156-8](https://doi:10.1016/S0304-3800(99)00156-8), 1999.

701 Chen, J. M., Mo, G., Pisek, J., Liu, J., Deng, F., Ishizawa, M., and Chan, D.: Effects of foliage clumping  
702 on the estimation of global terrestrial gross primary productivity, *Global Biogeochem. Cy.*, 26, GB1019,  
703 <https://doi.org/10.1029/2010GB003996>, 2012.

704 Chen, J., Ju, W., Ciais, P., Viovy, N., Liu, R., Liu, Y., and Lu X.: Vegetation structural change since 1981  
705 significantly enhanced the terrestrial carbon sink, *Nat. Commun.*, 10, 4259, [https://doi:10.1038/s41467-](https://doi:10.1038/s41467-019-12257-8)  
706 [019-12257-8](https://doi:10.1038/s41467-019-12257-8), 2019.

707 Chen, Z., Chen, J., Zhang, S., Zheng, X., Ju, W., Mo, G., Lu, X.: Optimization of Terrestrial Ecosystem  
708 Model Parameters Using Atmospheric CO<sub>2</sub> Concentration Data With the Global Carbon Assimilation  
709 System (GCAS), *J. GEOPHYS. RES. - BIOGEO.*, 122, 3218-3237,  
710 <http://doi.org/10.1002/2016JG003716>, 2017

711 Gough, C.: Terrestrial primary production: Fuel for life, *Nature Education Knowledge*, 3. 2012

712 Ham, Y., Choi, J., and Kug, J.: The weakening of the ENSO–Indian Ocean Dipole (IOD) coupling  
713 strength in recent decades, *Clim. Dynam.*, 49(1), 249-261, <https://doi:10.1007/s00382-016-3339-5>,  
714 2017.

715 He, B., Chen, C., Lin, S., Yuan, W., Chen, H., Chen, D., Zhang, Y., Guo, L., Zhao, X., Liu., Piao, S.,  
716 Zhong, Z., Wang, R., and Tang, R.: Worldwide impacts of atmospheric vapor pressure deficit on the  
717 interannual variability of terrestrial carbon sinks, *Natl. Sci. Rev.*, 9(4), nwab150,  
718 <https://doi:10.1093/nsr/nwab150>, 2022.

719 He, L., Chen, J., Liu, J., Bélair, S., and Luo, X.: Assessment of SMAP soil moisture for global simulation  
720 of gross primary production, *J. Geophys. Res. – Biogeo.*, 122(7), 1549-1563,  
721 <https://doi:10.1002/2016jg003603>, 2017.

722 He, L., Chen, J., Liu, J., Zheng, T., Wang, R., Joiner, J., Chou, S., Cheng, B., Liu, Y., and Liu, R.:  
723 Diverse photosynthetic capacity of global ecosystems mapped by satellite chlorophyll fluorescence  
724 measurements, *Remote Sens. Environ.*, 232, <https://doi:10.1016/j.rse.2019.111344>, 2019.

725 He, L., Chen J., Mostovoy, G., and Gonsamo, A.: Soil Moisture Active Passive Improves Global Soil  
726 Moisture Simulation in a Land Surface Scheme and Reveals Strong Irrigation Signals Over Farmlands,  
727 *Geophys. Res. Lett.*, 48(8), <https://doi:10.1029/2021gl092658>, 2021a.

728 He, L., Wang, R., Mostovoy, G., Liu, J., Chen, J., Shang, J., Liu, J., McNairn, H., and Powers, J.: Crop

729 Biomass Mapping Based on Ecosystem Modeling at Regional Scale Using High Resolution Sentinel-2  
730 Data, *Remote Sens.*, 13(4), <https://doi:10.3390/rs13040806>, 2021b.

731 He, Q., Ju, W., Dai, S., He, W., Song, L., Wang, S., Li, X., and Mao, G.: Drought Risk of Global  
732 Terrestrial Gross Primary Productivity Over the Last 40 Years Detected by a Remote Sensing-Driven  
733 Process Model. *J. Geophys. Res. – Biogeo.*, 126(6): e2020JG005944, 2021.

734 Hersbach, H., Bell, B., Berrisford, P., Biavati, G., Horányi, A., Muñoz Sabater, J., Nicolas, J., Peubey,  
735 C., Radu, R., Rozum, I., Schepers, D., Simmons, A., Soci, C., Dee, D., Thépaut, J-N.: ERA5 hourly  
736 data on single levels from 1940 to present, Copernicus Climate Change Service (C3S) Climate Data  
737 Store (CDS) [data set], [https://doi: 10.24381/cds.adbb2d47](https://doi:10.24381/cds.adbb2d47), 2023.

738 Houghton, R. A.: Balancing the global carbon budget, *Annu. Rev. Eart. Pl. Sc.*, 35, 313-347,  
739 <https://doi:10.1146/annurev.earth.35.031306.140057>, 2007.

740 [Humphrey, V., Zscheischler, J., Ciais, P., Gudmundsson, L., Sitch, S., and Seneviratne, SI.: Sensitivity](#)  
741 [of atmospheric CO<sub>2</sub> growth rate to observed changes in terrestrial water storage, \*Nature\*, 560\(7720\),](#)  
742 [628-631, 2018.](#)

743 [Humphrey, V., Berg, A., Ciais, P., Gentine, P., Jung, M., Reichstein, M., Seneviratne, SI., and](#)  
744 [Frankenberg, C.: Soil moisture–atmosphere feedback dominates land carbon uptake variability, \*Nature\*,](#)  
745 [592\(7852\), 65-69, 2021.](#)

746 [Jung, M., Reichstein, M., Schwalm, C. R., Huntingford, C., Sitch, S., Ahlstrom, A., Arneeth, A., Camps-](#)  
747 [Valls, G., Ciais, P., Friedlingstein, P., Gans, F., Ichii, K., Ain, A., Kato, E., Papale, D., Poulter, B., Raduly,](#)  
748 [B., Rödenbeck, C., Tramontana, G., Viovy, N., Wang, YP., Weber, U., Zaehle, S., and Zeng, N.:](#)  
749 [Compensatory water effects link yearly global land CO<sub>2</sub> sink changes to temperature, \*Nature\*, 541\(7638\),](#)  
750 [516-520, 2017.](#)

751 Joiner, J., Yoshida, Y., Zhang, Y., Duveiller, G., Jung, M., Lyapustin, A., Wang, Y., and Tucker, C. J.:  
752 Estimation of Terrestrial Global Gross Primary Production (GPP) with Satellite Data-Driven Models  
753 and Eddy Covariance Flux Data, *Remote Sens.*, 10(9), <https://doi:10.3390/rs10091346>, 2018.

754 Ju, W., Chen J., Black T., Barr, A., Liu, J., and Chen, B.: Modelling multi-year coupled carbon and  
755 water fluxes in a boreal aspen forest, *Agr. Forest Meteorol.*, 140(1-4), 136-151,  
756 <https://doi:10.1016/j.agrformet.2006.08.008>, 2006.

757 Fischer, G., Nachtergaele, F., Prieler, S., van Velthuizen, H. T., Verelst, L., Wiberg, D.: Global Agro-  
758 ecological Zones Assessment for Agriculture (GAEZ 2008), IIASA [data set], Laxenburg, Austria and  
759 FAO, Rome, Italy, 2008.

760 Friedl, M., Sulla-Menashe, D.: MCD12Q1 MODIS/Terra+Aqua Land Cover Type Yearly L3 Global  
761 500m SIN Grid V006, NASA EOSDIS Land Processes Distributed Active Archive Center [data set],  
762 2019.

763 Kim, J., Kug J., and Jeong S.: Intensification of terrestrial carbon cycle related to El Niño-Southern  
764 Oscillation under greenhouse warming, *Nat. Commun.*, 8, <https://doi:10.1038/s41467-017-01831-7>,  
765 2017.

766 Lan, X., Tans, P. and K.W. Thoning: Trends in globally-averaged CO<sub>2</sub> determined from NOAA Global  
767 Monitoring Laboratory measurements [data set], <https://doi.org/10.15138/9N0H-ZH07>, 2022.

768 Li, X., Cheng, G., Liu, S., Xiao, Q., Ma, M., Jin, R., Che, T., Liu, Q., Wang, W., Qi, Y., Wen, J., Li, H.,  
769 Zhu, G., Guo, J., Ran, Y., Wang, S., Zhu, Z., Zhou, J., Hu, X., Xu, Z.: Heihe watershed allied telemetry  
770 experimental research (HiWATER): scientific objectives and experimental design. *Bull. Am. Meteorol.*  
771 *Soc.* 94 (8), 1145–1160, <https://doi.org/10.1175/BAMS-D-12-00154.1>, 2013.

772 Li, Y., Dan, L., Peng, J., Wang, J., Yang, F., Gao, D., Yang, X., and Yu, Q.: Response of Growing Season  
773 Gross Primary Production to El Niño in Different Phases of the Pacific Decadal Oscillation over Eastern  
774 China Based on Bayesian Model Averaging, *Adv. Atmos. Sci.*, 38(9), 1580-1595,  
775 <https://doi:10.1007/s00376-021-0265-1>, 2021.

776 Liu, J., Chen J., Cihlar, J., and Park W.: A process-based boreal ecosystem productivity simulator using  
777 remote sensing inputs, *Remote Sens. Environ.*, 62(2), 158-175, [https://doi.org/10.1016/S0034-4257\(97\)00089-8](https://doi.org/10.1016/S0034-4257(97)00089-8), 1997.

779 Liu, Y., Liu, R., and Chen, J.: Retrospective retrieval of long-term consistent global leaf area index  
780 (1981-2011) from combined AVHRR and MODIS data. *J. Geophys. Res. Biogeosci.* 117 (G4), G04003,  
781 <https://doi.org/10.1029/2012JG002084>, 2012.

782 Liu, Y., Xiao, J., Ju, W., Zhu, G., Wu, X., Fan, W., Li, D., and Zhou, Y.: Satellite-derived LAI products  
783 exhibit large discrepancies and can lead to substantial uncertainty in simulated carbon and water fluxes,  
784 *Remote Sens. Environ.*, 206, 174-188, <https://doi:10.1016/j.rse.2017.12.024>, 2018.

785 Liu, Y., Yang X., Wang, E., and Xue, C.: Climate and crop yields impacted by ENSO episodes on the  
786 North China Plain: 1956-2006, *Reg. Environ. Change.*, 14(1), 49-59, [https://doi:10.1007/s10113-013-](https://doi:10.1007/s10113-013-0455-1)  
787 0455-1, 2014.

788 Mercado, L., Bellouin, N., Sitch, S., Boucher, O., Huntingford, C., Wild, M., Cox, P.: Impact of changes  
789 in diffuse radiation on the global land carbon sink, *Nature*, 458(7241), 1014-1017,  
790 <https://doi:10.1038/nature07949>, 2009.

791 Muñoz, S. J.: ERA5-Land monthly averaged data from 1950 to present. Copernicus Climate Change  
792 Service (C3S) Climate Data Store (CDS) [data set], 2019.

793 Norman, J. M.: Simulation of microclimates, in: *Biometeorology in Integrated Pest Management*, edited  
794 by: Hatfield, J., Thomason, I., 65–99, New York, CA: Academic Press, 1982.

795 [Piao, S., Sitch, S., Ciais, P., Friedlingstein, P., Peylin, P., Wang, X., Ahlstrom, A., Anav, A., Canadell,](#)  
796 [J., Cong, N., Huntingford, C., Jung, M., Levis, S., Levy, PE., Li, J., Lin, X., Lomas, M., Lu, M., Luo,](#)  
797 [Y., Ma, Y., Myneni, R., Poulter, B., Sun, Z., Wang, T., Viovy, N., Zaehle, S., and Zeng, N.: Evaluation](#)  
798 [of terrestrial carbon cycle models for their response to climate variability and to CO<sub>2</sub> trends. \*Global\*](#)  
799 [Change Biol., 2117–2132, 2013.](#)

800 Piao, S., Wang, X., Wang, K., Li, X., Bastos, A., Canadell, J., Ciais, P., Friedlingstein, P., and Sitch, S.:  
801 Interannual variation of terrestrial carbon cycle: Issues and perspectives, *Global Change Biol.*, 26(1),  
802 300-318, <https://doi:10.1111/gcb.14884>, 2020.

803 Ryu, Y., Berry J., and Baldocchi, D.: What is global photosynthesis? History, uncertainties and  
804 opportunities, *Remote Sens. Environ.*, 223, 95-114, <https://doi:10.1016/j.rse.2019.01.016>, 2019.

805 Saji, N., Goswami, B, Vinayachandran P, and Yamagata, T.: A dipole mode in the tropical Indian Ocean,  
806 *Nature*, 401(6751), 360-363, <https://doi:10.1038/43855>, 1999.

807 Saji, N., and Yamagata, T.: Possible impacts of Indian Ocean Dipole mode events on global climate,  
808 *Clim. Res.*, 25(2), 151-169, <https://doi:10.3354/cr025151>, 2003.

809 Sanders-DeMott, R., Ouimette, A., Lepine, L., Fogarty, S., Burakowski, E., Contosta, A., Ollinger, S.:  
810 Divergent carbon cycle response of forest and grass-dominated northern temperate ecosystems to record  
811 winter warming. *Global Change Biol.*, 26(3): 1519-1531, <https://doi.org/10.1111/gcb.14850>, 2020.

812 Schimel, D., Stephens, B., and Fisher, J.: Effect of increasing CO<sub>2</sub> on the terrestrial carbon cycle, P.

813 Natl. Acad. Sci. USA., 112(2), 436-441, <https://doi:10.1073/pnas.1407302112/-/DCSupplemental>,  
814 2015.

815 Wang, J., Zeng, N., and Wang, M.: Interannual variability of the atmospheric CO<sub>2</sub> growth rate: roles of  
816 precipitation and temperature, *Biogeo.*, 13(8), 2339-2352, <https://doi:10.5194/bg-13-2339-2016>, 2016.

817 Wang, J., Zeng, N., Wang, M., Jiang, F., Chen, J., Friedlingstein, P., Jain, A., Jiang, Z., Ju, W., Lienert,  
818 S., Nabel, J., Sitch, S., Viovy, N., Wang, H., and Wiltshire, A.: Contrasting interannual atmospheric CO<sub>2</sub>  
819 variabilities and their terrestrial mechanisms for two types of El Niños, *Atmos. Chem. Phys.*, 18(14),  
820 10333-10345, <https://doi:10.5194/acp-18-10333-2018>, 2018.

821 Wang, J., Liu, Z., Zeng, N., Jiang, F., Wang, H., and Ju, W.: Spaceborne detection of XCO<sub>2</sub> enhancement  
822 induced by Australian mega-bushfires, *Environ. Res. Lett.*, 15(12), [https://doi:10.1088/1748-](https://doi:10.1088/1748-9326/abc846)  
823 9326/abc846, 2020.

824 Wang, J., Jiang, F., Wang, H., Qiu, B., Wu, M., He, W., Ju, W., Zhang, Y., Chen, J., and Zhou, Y.:  
825 Constraining global terrestrial gross primary productivity in a global carbon assimilation system with  
826 OCO-2 chlorophyll fluorescence data, *Agr. Forest Meteorol.*, 304-305,  
827 <https://doi:10.1016/j.agrformet.2021.108424>, 2021a.

828 Wang, J., et al.: Modulation of Land Photosynthesis by the Indian Ocean Dipole: Satellite-Based  
829 Observations and CMIP6 Future Projections, *Earth's Future*, 9(4), <https://doi:10.1029/2020ef001942>.  
830 2021b.

831 Wang, M., Wang, J., Cai, Q., Zeng, N., Lu, X., Yang, R., Jiang, F., Wang, H., and Ju, W.: Considerable  
832 Uncertainties in Simulating Land Carbon Sinks Induced by Different Precipitation Products, *J. Geophys.*  
833 *Res. - Biogeo.*, 126(10), e2021JG006524, <https://doi.org/10.1029/2021JG006524>. 2021c

834 Wang, J., Jiang, F., Ju, W., Wang, M., Sitch, S., Arora, V., Chen, J., Goll, D., He, W., Jain, A., Li, X.,  
835 Joiner, J., Poulter, B., Seferian, R., Wang, H., Wu, M., Xiao, J., Yuan, W., Yue, X., Zaehle, S.: Enhanced  
836 India-Africa Carbon Uptake and Asia-Pacific Carbon Release Associated With the 2019 Extreme  
837 Positive Indian Ocean Dipole, *Geophys. Res. Lett.*, 49(22), <https://doi:10.1029/2022gl100950>, 2022.

838 Wang, J., et al.: Anomalous Net Biome Exchange Over Amazonian Rainforests Induced by the 2015/16  
839 El Niño: Soil Dryness-Shaped Spatial Pattern but Temperature-dominated Total Flux, *Geophys. Res.*  
840 *Lett.*, 50(11), <https://doi:10.1029/2023GL103379>, 2023.

841 Williams, C., and Hanan, N.: ENSO and IOD teleconnections for African ecosystems: evidence of  
842 destructive interference between climate oscillations, *Biogeo.*, 8(1), 27-40, [https://doi:10.5194/bg-8-](https://doi:10.5194/bg-8-27-2011)  
843 27-2011, 2011.

844 Yan, R., Wang, J., Ju, W., Goll, D., Jain, A., Sitch, S., Tian, H., Benjamin, P., Jiang, F., and Wang, H.:  
845 Interactive effects of the El Niño-Southern Oscillation and Indian Ocean Dipole on the tropical net  
846 ecosystem productivity, *Agr. Forest Meteorol.*, 336, 109472,  
847 <https://doi.org/10.1016/j.agrformet.2023.109472>, 2023.

848 Yang, R., Wang, J., Zeng, N., Sitch, S., Tang, W., McGrath, M., Cai, Q., Liu, D., Lombardozzi, D., Tian,  
849 H., Jain, A., and Han, P.: Divergent historical GPP trends among state-of-the-art multi-model  
850 simulations and satellite-based products, *Earth Syst. Dynam.*, 13(2), 833-849, [https://doi:10.5194/esd-](https://doi:10.5194/esd-13-833-2022)  
851 13-833-2022, 2022.

852 Yang, Y., S.-P. Xie, L. Wu, Y. Kosaka, N.-C. Lau, and G. A. Vecchi, 2015: Seasonality and Predictability  
853 of the Indian Ocean Dipole Mode: ENSO Forcing and Internal Variability, *J. Climate*, 28(20), 8021-  
854 8036, <https://doi:10.1175/JCLI-D-15-0078.1>.

855 Ying, K., Peng, J., Dan, L., and Zheng, X.: Ocean—atmosphere Teleconnections Play a Key Role in the  
856 Interannual Variability of Seasonal Gross Primary Production in China, *Adv. Atmos. Sci.*, 39(8), 1329-  
857 1342, <https://doi:10.1007/s00376-021-1226-4>, 2022.

858 Zeng, N., Mariotti, A., and Wetzel, P.: Terrestrial mechanisms of interannual CO<sub>2</sub> variability, *Global*  
859 *Biogeochem Cy.*, 19(1), <https://doi:10.1029/2004gb002273>, 2005.

860 Zhang, X., Wang, Y., Peng, S., Rayner, P., Ciais, P., Silver, J., Piao, S., Zhu, Z., Lu, X., Zheng, X.:  
861 Dominant regions and drivers of the variability of the global land carbon sink across timescales, *Global*  
862 *Change Biol.*, 24(9), 3954-3968, <https://doi:10.1111/gcb.14275>, 2018.

863 Zhang, Y., Dannenberg, M., Hwang, T., and Song, C.: El Niño-Southern Oscillation-Induced Variability  
864 of Terrestrial Gross Primary Production During the Satellite Era, *J. Geophys. Res. - Biogeo.*, 124(8),  
865 2419-2431, <https://doi:10.1029/2019jg005117>, 2019.

866 Zhang, Y., Zhou, W., Wang, X., Wang, X., Zhang, R., Li, Y., and Gan, J.: IOD, ENSO, and seasonal  
867 precipitation variation over Eastern China, *Atmos. Res.*, 270,  
868 <https://doi:10.1016/j.atmosres.2022.106042>, 2022a.



869 Zhang, Y., Zhou, W., Wang, X., Chen, S., Chen, J., and Li, S.: Indian Ocean Dipole and ENSO's  
870 mechanistic importance in modulating the ensuing-summer precipitation over Eastern China, *NPJ Clim.*  
871 *Atmos. Sci.*, 5(1), <https://doi:10.1038/s41612-022-00271-5>, 2022b.

872 Zhu, Z., Piao, S., Xu, Y., Bastos, A., Ciais, P., and Peng, S.: The effects of teleconnections on carbon  
873 fluxes of global terrestrial ecosystems, *Geophys. Res. Lett.*, 44(7), 3209-3218,  
874 <https://doi:10.1002/2016GL071743>, 2017.